Improved Boundary Segmentation of Skin Lesions in High-Frequency 3D Ultrasound

B Sciolla, P Delachartre

CREATIS, INSA Lyon, France

L Cowell

Melanoma Skin Cancer Clinic, Hamilton Hill, Australia

T Dambry, B Guibert

Atys Medical, Soucieu-En-Jarrest, France

Abstract

In this article, we propose a segmentation algorithm for skin lesions in 3D high-frequency ultrasound images. The segmentation is done on melanoma and Basal-cell carcinoma tumors, the most common skin cancer types, and could be used for diagnosis and surgical excision planning in a clinical context. Compared with previously proposed algorithms, which tend to underestimate the size of the lesion, we propose two new boundary terms which provide significant improvements of the accuracy. The first is a probabilistic boundary expansion (PBE) term designed to broaden the segmented area at the boundaries, which uses the feature asymmetry criterion. The second is a curvature dependent regularization (CDR), which aims at overcoming the tendency of standard regularization to shrink segmented areas. On a clinical dataset of 12 patients annotated by a dermatologist, the proposed algorithm has a comparable Dice index but increases the sensitivity by 26%. The proposed algorithm improves the sensitivity for all lesions, and the obtained sensitivity is close to that of the intra-observer variability.

Keywords: Segmentation, Level-set, curvature-driven dynamics, Feature asymmetry, tumor, melanoma, Basal-cell Carcinoma, ultrasound

*CREATIS, Bat. 502, 7 av. Jean Capelle, 69621 VILLEURBANNE, France

Email address: bruno.sciolla@creatis.insa-lyon.fr, +33472438226 (B Sciolla, P Delachartre)

1. Introduction

In this article, we focus on the problem of segmentation of lesions in 3D high-frequency ultrasound images. The lesions considered are the two most common types of skin cancer lesions, melanoma and Basal-Cell Carcinoma (BCC). Skin cancer is the most common type of cancer by far, accounting for approximately 76% of all cancers [1, 2] (this and the following are statistics measured in the United States). One in five individuals will develop skin cancer during their lifetime [3]. The annual cost of treating skin cancer is of $ 8.1 billion per year. Melanoma is among the most frequent cancers associated with high morbidity, totaling 4.5% of all diagnosed cancers [2]. For melanoma, early diagnosis is a crucial factor. For early diagnosed stage IA melanoma, the 10-year survival rate is of 93%, whereas for late diagnosis stage IIC melanoma the survival rate is of 39% only [4]. BCC is the most widespread skin cancer. Every individual has on average a 6.0% (age-adjusted) chance of developing BCC per year [1]. BCC has a much lower morbidity than melanoma, but the surgical treatment has high recurrence rates [5].

Although dermoscopic evaluation and biopsy is the most used diagnosis tool in dermatology, a number of noninvasive modalities are available to monitor the skin, such as reflectance confocal microscopy [6] or optical coherence tomography [7]. In this article, we focus on high-frequency ultrasound, which have several advantages such as providing 2D or 3D images in short times and is comparatively lightweight and less costly. Moreover, ultrasound can probe at depths of 3 mm or more, while optical coherence tomography and reflectance confocal microscopy are limited to a depth of 500 μm, which is insufficient to scan the bottom of deep lesions. Nevertheless, 3D ultrasound is not widely used in clinical practice at the moment, in particular due to the lack of processing tools for the 3D images.

Obtaining 3D segmentation of skin lesions has a number of clinical applications. For Basal-Cell Carcinoma, determining the spatial extent of a the lesion is a crucial issue for the surgical excision [8]. Indeed, in standard excision surgery, the clinician has little information on the exact horizontal and in-depth extent of the lesion. Large margins are used to ensure the removal of all malignant tissues. Despite these protocols, recurrence rates in standard surgery can be as high as 12.2% for basal cell carcinoma situated on the face [9]. It has been shown that high-frequency ultrasound provide good estimators of the tumor depth [10] and extents [8, 11, 12] for basal-cell carcinomas. Quantitative 3D segmentation may improve the success of standard surgical excision and avoid resorting to more expensive methods like Mohs' Micrographic surgery [9]. For the melanoma, the segmentation in 3D can be an adjunct to diagnosis, the shape of the lesion being related with malignancy [13]. It can also serve for biopsy site selection, or the assessment of treatment response, Confocal Reflectance Microscopy is used in a similar way [6]. The problem with the diagnosis of melanoma is to reliably detect malignant lesions among a large number of benign naevi. A lot of research effort is spend to improve the clinical diagnosis using existing or new imaging methods such as dermoscopy, reflectance confocal microscopy, total body photography,

multispectral imaging and even smartphone applications [14, 15]. The development of automatic segmentation tools is a part of this effort. In particular, several segmentation tools have been proposed for dermoscopic images [16, 13].

The most recently proposed algorithms for the segmentation of lesions in 3D ultrasound images are [17, 18]. Reference [17] is based on Markov Random Fields, and has large computation times. The state-of-the-art intensity-based 3D level-set method for the segmentation of lesions in 3D ultrasound images is [18].

However, these algorithms lack accuracy at the boundaries of the lesions, and tend to underestimate the size of the tumors. The first cause of the inaccuracy is that, close to the boundary of a tumor, the intensity is gradually increasing from pathological to normal tissue. As a result, the algorithms proposed previously tend to place the boundary in the middle between hypoechoic tissues and normal tissues, whereas in reality the tumor is formed of all anomalous tissues. The second cause of the lack of accuracy is the regularization term in the level-set, which causes a curvature driven dynamics [19] during the optimization. Although this term is necessary to regularize the contour, it tends to unnecessarily shrink the segmented area. In the following, we propose two improvements to address these problems:

1. The first is a Probabilistic Boundary Expansion (PBE) term based on a conditional maximum likelihood estimate. This term is specifically designed to only increase the extents of the segmented area at the boundary. This term counter-balances the gradual increase of intensity at the boundary of the lesion, and allows the segmentation of the entire lesion.
2. The second contribution is to replace standard regularization with a Curvature-Dependent Regularization (CDR) term. This term alleviates the problem of curvature-driven dynamics, while still ensuring that the contour is smooth and regular.

We now describe previous works related to the proposed terms. The PBE uses a Feature Asymmetry (FA) map [20] computed from the monogenic signal [21]. The Feature Asymmetry is a powerful edge detector for ultrasound images and has been used successfully in several segmentation tasks [22, 23]. Reference [23] features a non-parametric intensity-based criterion with an additional feature asymmetry boundary term. Reference [24] introduces a phase-based boundary term for the segmentation of 3D ultrasound images.

The second term, curvature dependent regularization (CDR), is a variant of front-propagation algorithms, such as min/max curvature flow [19]. It is a natural solution to a well-known effect, the curvature-driven dynamics, which tends to shrink the segmented area. Previously, this problem was treated using heuristic terms such as ballooning forces which are still sometimes used [25]. However, such methods introduce an additional parameter, which is difficult to choose consistently. In our method, the parameters have a direct geometric meaning. The proposed curvature-dependent regularization is also formally related with anisotropic diffusion [26, 27].

The rest of the paper is organized as follows: section 2 describes the proposed PBE and CDR terms, section 3 presents a comparison of the proposed method with previous methods used in the literature, namely the intensity-based log-likelihood method [18] and Geometric Active Contours (GAC) [23]. The comparison is conducted on a clinical dataset of 9 melanoma and 3 basal cell carcinoma. The accuracy is measured using the Dice index, the precision, the sensitivity and the Mean Absolute Distance with respect to two reference contours drawn by the expert. The results are discussed in section 4 and a conclusion follows in section 5.

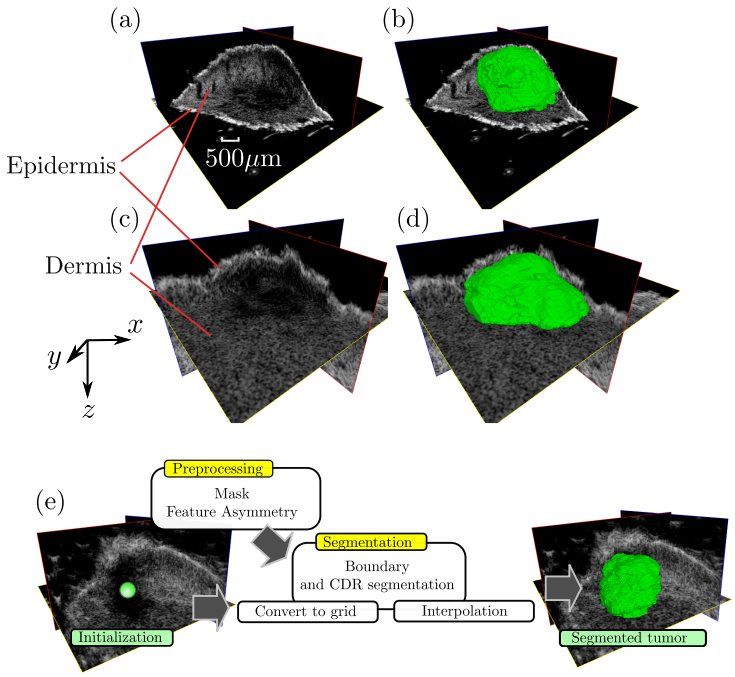

Figure 1: 3D ultrasound images of two melanoma lesions. **(a), (c)** Images of the lesions, showing the epidermis (hyperechoic) and the dermis. The tumors appear as an inhomogeneous hypoechoic area with blurred boundaries. **(b) , (d)** Automatic segmentation of the lesions. **(e)** Overview of the processing chain. The user gives a seed point inside the lesion. The feature asymmetry map is computed, and a mask excluding the area above the skin is defined using a preliminary level-set segmentation. The segmentation takes place on a grid for faster computation, and after convergence the result is interpolated to the original grid size.

2. Materials and Methods

2.1. 3D high-frequency ultrasound images of tumors

Figure 1 (a-d) depicts 3D ultrasound images of the dermis and the corresponding segmentation of the tumor, which is visible as a hypoechoic and inhomogeneous area in the dermis. The axis z spans the depth of the skin, and

the (x, y) coordinates span the planes parallel to the surface of the epidermis. The black area above the epidermis is the ultrasound gel applied on the skin for the acquisition. The gel area is excluded using a pre-segmentation procedure, it is called Mask in the processing chain of Fig. 1(e).

2.2. Objective function

The proposed segmentation method is based on a hybrid geodesic active contour, which contains both an area term and boundary terms. The area term measures the log-likelihood of the intensity [18], to which we add the proposed two boundary terms. The image volume X is partitioned into two regions A and B, according to the sign of the function $\phi_{\mathbf{x}} = \phi(\mathbf{x})$, where $\mathbf{x}$ represents the coordinates of a point in the image. Specifically, the region of interest is $A = \{\mathbf{x} \in X | \phi_{\mathbf{x}} > 0\}$ and the background is $B = \{\mathbf{x} \in X | \phi_{\mathbf{x}} \leq 0\}$, separated by a boundary ∂A. The segmented area is obtained from a minimizer $\phi_{\mathbf{x}}$ of an objective function $E[\phi]$:

$$E^{\text{proposed}}[\phi] \quad = \alpha E^{\text{int}}[\phi] + \beta E^{\text{PBE}}[\phi] + \gamma E^{\text{CDR}}[\phi] \tag{1}$$

which contains a log-likelihood term discriminating the intensity $E^{\text{int}}[\phi]$, a boundary term $E^{\text{PBE}}[\phi]$ and an curvature dependent regularization $E^{\text{CDR}}[\phi]$, weighted by three parameters α, β and γ. The two terms $E^{\text{PBE}}[\phi]$ and $E^{\text{CDR}}[\phi]$ are the original contributions of this article.

For completeness, we recall that the log-likelihood term for the intensity is [18, 28]:

$$E^{\text{int}}[\phi] \quad = -\int_A \log \hat{P}(I_{\mathbf{x}}|A)\mathrm{d}\mathbf{x} - \int_B \log \hat{P}(I_{\mathbf{x}}|B)\mathrm{d}\mathbf{x} \tag{2}$$

where $\hat{P}(I|A)$ is the estimate of the distribution of intensity I in the region A, obtained via a Parzen estimate during the minimization process. Since this term uses the full empirical distribution of the intensity, all moments of the local intensity play a role. This term is thus a rich local texture criterion. We now describe the two boundary terms.

2.3. Probabilistic Boundary Expansion (PBE) term based on the Feature Asymmetry (FA)

We compute a Feature Asymmetry (FA) map from the monogenic signal as described in [22]. Before computing the FA map, images are first denoised using complex wavelets [29] with a thresholding of fixed threshold $T = 40$ for images normalized in the range [0,255]. The feature asymmetry map provides reliable information on the boundary of a lesion, as depicted in Fig. 2(a, b). It can be observed that the FA map takes nonzero values in the blurry transition area between the dark lesion and the surrounding tissue. Qualitatively, the contour should extend as far as possible into the boundary area, to avoid underestimating the extent of the lesion.

Previously, it was proposed [23] to use the feature asymmetry in a geometric active contour (GAC) [30] boundary term $E^{\text{GAC}}[\phi] = \int_{\partial A} g_{\mathbf{x}}^{\text{GAC}} d\mathbf{x}$, with

$g_{\mathbf{x}}^{\mathrm{GAC}} = 1/(\epsilon + \mathrm{FA}_{\mathbf{x}})$ (with a hyperparameter ϵ). With this method, the contour is driven towards the maxima of the feature asymmetry, as depicted in Fig. 2(c). The study [24] also introduces a similar boundary term which drives the contour towards maxima of the feature asymmetry. In the following, we compare the proposed method to the (GAC) segmentation of Ref. [23]. The (GAC) segmentation is the minimizer of $\alpha E^{\mathrm{int}}[\phi] + \beta E^{\mathrm{GAC}}[\phi]$. Our tests have shown that without an area term, like in [24], a correct segmentation of lesions can not be obtained.

In this article, we propose instead a probabilistic boundary expansion term (PBE) based on a maximum a posteriori objective function $E^{\mathrm{PBE}}[\phi]$ which always tends to make the contour extend within the boundary area as shown in Fig. 2(d), which suits our application better. The qualitative idea is that in the area where the Feature Asymmetry is nonzero, the boundary should be allowed to expand. To express this objective formally, we comply with the maximum log-likelihood framework used for the intensity $E^{\mathrm{int}}[\phi]$. The PBE objective is written as a maximum a posteriori log-likelihood of having value FA of the feature asymmetry, given that the FA is strictly positive. Let us call $\hat{P}(\mathrm{FA}|A, \mathrm{FA}_{\mathbf{x}} > 0)$ the conditional probability distribution of the FA, given that the point of interest $\mathbf{x}$ is in region A and that the feature Asymmetry $\mathrm{FA}_{\mathbf{x}}$ is strictly positive. The PBE objective function quantifies the log-likelihood of having value FA of the feature asymmetry, given that the FA is strictly positive, and reads:

$$E^{\mathrm{PBE}}[\phi] = -\int_A \theta(\mathrm{FA}_{\mathbf{x}}) \log\left(\hat{P}(\mathrm{FA}_{\mathbf{x}}|A)\right) \mathrm{d}\mathbf{x} - \int_B \theta(\mathrm{FA}_{\mathbf{x}}) \log\left(\hat{P}(\mathrm{FA}_{\mathbf{x}}|B)\right) \mathrm{d}\mathbf{x} \quad (3)$$

where θ is the Heaviside function $\theta(x) = 0$ for $x \leq 0$; $\theta(x) = 1$ for $x > 0$. This term does not alter the contour position in regions with $\mathrm{FA}_{\mathbf{x}} = 0$ and increases the likelihood of regions with nonzero $\mathrm{FA}_{\mathbf{x}}$ to be inside of the contour A. For the sake of simplicity, the ratio $\hat{P}(\mathrm{FA}_{\mathbf{x}}|A)/\hat{P}(\mathrm{FA}_{\mathbf{x}}|B)$ is supposed to be constant.

2.4. Curvature-dependent regularization (CDR)

The second boundary term that we propose is a curvature dependent regularization term.

$$E^{\mathrm{CDR}}[\phi] \quad = \int_{\partial A} g_{\mathbf{x}} \, \mathrm{d}\mathbf{x} \quad (4)$$

The gradient descent for the general case (4) is [30]:

$$\partial_t \phi_{\mathbf{x}} = \delta(\phi_{\mathbf{x}}) \, \mathrm{div}\left(g_{\mathbf{x}} \frac{\nabla \phi_{\mathbf{x}}}{|\nabla \phi_{\mathbf{x}}|}\right) \quad (5)$$

where δ is the Dirac delta distribution. The standard regularization [31] term is obtained from (4) or (5) with $g_{\mathbf{x}} = 1$. This term produces a curvature-driven boundary evolution [19], as illustrated in Fig. 3(a, b). This equation can also be understood as a front propagation $\partial_t n = -\kappa_{\mathbf{x}}$ where n is the displacement along the direction normal to the interface, and $\kappa_{\mathbf{x}} = \mathrm{div}\,(\nabla \phi_{\mathbf{x}}/|\nabla \phi_{\mathbf{x}}|)$ is the local mean curvature of the boundary. This dynamics typically causes a collapse

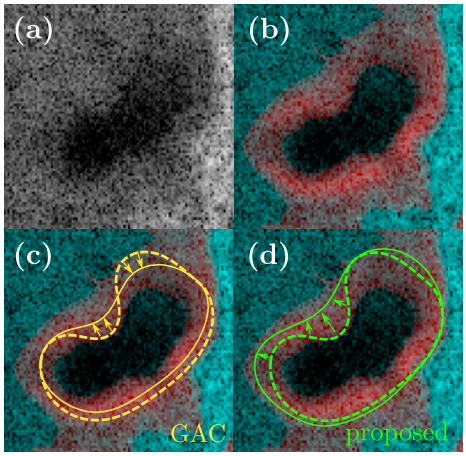

Figure 2: **(a)** x-y slice of a tumor and **(b)** Feature Asymmetry map is superimposed in red. Specifically, the RGB channels of the image shown are set to $I^R_{\mathbf{x}} = \mathrm{FA}_{\mathbf{x}}/\max_{\mathbf{x}}(\mathrm{FA}_{\mathbf{x}})$, $I^G_{\mathbf{x}} = I^B_{\mathbf{x}} = I_{\mathbf{x}}/\max_{\mathbf{x}}(I_{\mathbf{x}})$ **(c)** Qualitative action of the GAC contour segmentation. Dashed line: contour at step t. Solid line, contour at step $t + \Delta t$. With GAC, the contour tends to go through the maxima of the feature map, which can shrink or extend the segmented area. **(d)** Qualitative action of the proposed PBE term, with the same conventions. With the proposed method, the contour tends to include more and more regions with nonzero feature map, which always makes the contour extend to include the margins. For the problem at hand, this is the preferred behavior.

of the smallest region. One can compute analytically the collapse of a spherical region in 3D, of radius $r(t)$, with initial radius r_0. The sphere is parametrized using $\phi(r) = r - r(t)$ in spherical coordinates (r, θ, ϕ). The local curvature is given by $\kappa(r) = 2/r$, so that the evolution of the radius of the sphere $r(t)$ is $\partial_t r(t) = -2/r(t)$, with solution $r(t) = \sqrt{r_0^2 - 4t}$. The sphere collapses to a point in a time $t^* = r_0^2/4$. The collapse of a sphere and the evolution of the radius as a function of time is shown in Fig. 3(a, b). The curvature-driven motion, which is used in the normal segmentation, is one of the causes of underestimation of the tumor size.

We propose instead a curvature-dependent regularization (CDR). With CDR, the curvature motion only takes place when the local curvature $\kappa_{\mathbf{x}}$ is above a certain threshold κ_0. The curvature-dependent evolution is obtained by setting

$$g_{\mathbf{x}} = 1 - \frac{1}{1 + \exp\left(\lambda\left(|\kappa_{\mathbf{x}}| - \kappa_0\right)/\kappa_0\right)} \tag{6}$$

which has the property $g_{\mathbf{x}} \sim 0$ for $\kappa_{\mathbf{x}} \lesssim \kappa_0$ and $g_{\mathbf{x}} \sim 1$ for $\kappa_{\mathbf{x}} \gtrsim \kappa_0$. These properties are exact in the limit $\lambda \to \infty$. The parameter κ_0 defines the minimal curvature expected for the target segmentation, or equivalently the inverse of the expected length-scale of the roughness. The parameter λ defines the range of curvature across which the regularization sets in. Figure 3(c, d) illustrates the CDR curvature motion on a sphere, in the limit $\lambda \to \infty$. Figure 3(e) shows

the CDR curvature motion on rectangular shape. Figure 3(f) illustrates the dynamics of the curvature motion with standard regularization and with CDR, and Fig. 3(g) illustrates a single line with curvature above, equal and below the threshold curvature κ_0. The figures show that the CDR makes the contour smooth without shrinking the segmented area. In this sense, the CDR term improves the sensitivity compared with standard regularization.

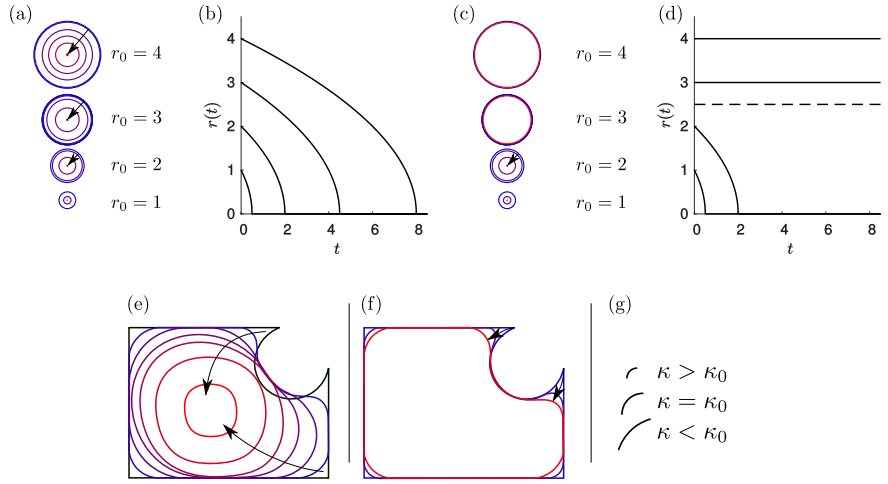

Figure 3: **(a-d)** Dynamics induced by the regularization term for four spherical areas of initial radius $r_0 = \{1, 2, 3, 4\}$. In **(a), (b)**, the standard regularization $g_{\mathbf{x}} = 1$ is used. In **(c), (d)**, the curvature-dependent regularization is used, in the limit $\lambda \to \infty$. **(a), (c)** Depicts the contour at several times from dark blue to light red. The direction of the curvature motion is indicated by the arrows. **(b), (d)** Shows the evolution of the radius $r(t)$ as a function of time t. Standard regularization. All shapes collapse to a point. **(b)** With standard regularization, all spheres collapse to a point in a finite time. **(d)** With CDR, all spheres of radius $r > r^*$ are stable, and all spheres with $r < r^*$ collapse. The critical radius $r^* = 2/\kappa_0$ is equal to $r^* = 2.5$, and shown as a dashed line. **(e-g)** Dynamics induced by the regularization term for an initial contour with a rectangle with a hole (black line). The evolution is depicted by the arrows and the colors from dark blue to light red. **(e)** Standard regularization. The shape collapses to a point in a finite time. **(f)** CDR curvature motion. Contours with a low curvature $\kappa < \kappa_0$ are stable. **(g)** Example of lines with different curvatures, respectively higher, equal to and less than κ_0. Smoothing in case (f) occurs only for $\kappa > \kappa_0$.

2.5. Processing chain

The global processing chain of the clinical data is shown in Fig. 1(e). The user provides a seed point inside the tumor which is used to initialize the contour. The feature asymmetry is then computed, along with a mask which restricts the segmentation to the volume inside the skin. The actual level-set optimization takes place on a coarse rectangular grid of size $3 \times 3 \times 6$ pixels, or $160 \times 160 \times 22$ μm, to save processing time, and the result is interpolated to obtain the final segmented volume. The grid size has been chosen to have a minor impact on the accuracy. Specifically, we compare the accuracy of pixelwise and grid

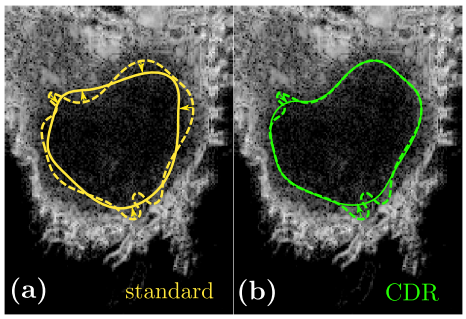

Figure 4: Dynamics induced by the regularization term in a tumor. Dashed line: contour at step t. Solid line, contour at step $t + \Delta t$. **(a)** Standard regularization. The rough parts of the contour are smoothed. Yet, due to the curvature motion, the segmentation shrinks even in areas which are already smooth. **(b)** CDR regularization. The contour is regularized, but the lesion is not shrunk.

segmentation to the reference contours, for decreasing grid sizes, until a plateau is reached. The use of the grid decreases the computing time by a factor of 100.

The gradient descent for the energy in Eq. (1) reads:

$$\partial_t \phi_{\mathbf{x}} = \delta(\phi_{\mathbf{x}}) \left(\alpha f^{\text{int}}_{\mathbf{x}} + \beta f^{\text{PBE}}_{\mathbf{x}} + \gamma f^{\text{CDR}}_{\mathbf{x}}\right) \tag{7}$$

$$f^{\text{CDR}}_{\mathbf{x}} = \text{div}\left(g_{\mathbf{x}} \frac{\nabla \phi_{\mathbf{x}}}{|\nabla \phi_{\mathbf{x}}|}\right) \tag{8}$$

$$f^{\text{int}}_{\mathbf{x}} = \log\left(\frac{\hat{P}(I_{\mathbf{x}}|A)}{\hat{P}(I_{\mathbf{x}}|B)}\right) \qquad f^{\text{PBE}}_{\mathbf{x}} = \theta(\text{FA}_{\mathbf{x}}) \log\left(\frac{\hat{P}(\text{FA}_{\mathbf{x}}|A)}{\hat{P}(\text{FA}_{\mathbf{x}}|B)}\right) \tag{9}$$

where $\delta(.)$ is the Dirac delta distribution and θ is the Heaviside function. The minimization is performed using a gradient descent with a semi-implicit solver described in detail in Appendix A.

3. Results

3.1. Clinical data acquisition

Images in the dataset were acquired with a 50 MHz Dermcup 3D imaging system, Atys Medical (Soucieu-en-Jarrest, France) at the Melanoma Skin Cancer Clinic, Hamilton Hill, Australia. The probe makes 3D ultrasound images of size 16×16×3.12 mm (last is depth inside the skin), for a size of 300 × 299 × 832 voxels. The lateral resolution is of 50 μm and the axial (depth) resolution is of 25 μm. The clinical cases include 3 basal cell carcinoma (BCC) and 9 melanoma. Both types of lesion are hypoechoic in ultrasound images, but the melanoma has a much higher contrast than the BCCs. Although the dataset is small, the different lesions are representative of the diversity of cases encountered in a clinical setting. Moreover, the dataset of 12 cases of 3D images is equivalent to 1800 2D images. This study is retrospective chart research on images for which written consent was obtained.

The algorithm is implemented in Matlab, with low-level C++ subroutines for improved speed. A segmentation takes on average 40 s on a single machine with an Intel i7-4770 processor. The segmented region is in a window centered on the lesion, the window is on average of size $150 \times 150 \times 400$ voxels, approximately 9 millions voxels.

3.2. Metrics

The performance of the segmentation was evaluated with respect to the two expert reference contours R_1 and R_2 made by a dermatologist. The reference contours R_1 are made in $z-x$ parallel planes, whereas the R_2 contours are made on $y-z$ planes. This allowed estimation of the intra-operator variability, for example computing $D(R_1|R_2)$ and $D(R_2|R_1)$.

In the following, we use several similarity measures to assert the accuracy of the segmented contours. If $\Omega = A$ is the segmented volume, and R the reference volume, the sensitivity $S(\Omega|R) = |\Omega \cap R|/|R|$ is the true positive rate over the reference area, the precision is $P(\Omega|R) = |\Omega \cap R|/|\Omega|$ the true positive rate over the segmented area. The Sørensen-Dice index is $D(\Omega|R) = 2|\Omega \cap R|/(|\Omega| + |R|)$. The Dice index D can also be expressed as the harmonic mean of sensitivity S and precision P, $D = 2/(1/S + 1/P)$. The (symmetric) Mean Absolute Distance $\mathrm{MAD}(\Omega|R)$ is an average distance between the segmented contour and the reference:

$$\mathrm{MAD}(\Omega|R) = \sum_{\mathbf{x}\in\partial\Omega} \frac{d(\mathbf{x}|R)}{2\ \mathrm{surf}(\partial\Omega)} + \sum_{\mathbf{x}\in\partial R} \frac{d(\mathbf{x}|\Omega)}{2\ \mathrm{surf}(\partial R)} \tag{10}$$

where $d(\mathbf{x}|R) = \min_{\mathbf{x}'\in\partial R} \|\mathbf{x}' - \mathbf{x}\|$ is the distance of point $\mathbf{x}$ to the reference contour ∂R. $\mathrm{surf}(\partial R)$ is the number of pixels in the boundary ∂R. The MAD is measured in μm. In the following, the accuracy indicators D, S, P and MAD are measured with respect to R_1, then to R_2. In the following, all results $D(\Omega|R_1)$, $D(\Omega|R_2)$ are considered as two independent points. For example, for a given segmentation method, one obtains 12 segmented regions Ω on the 12 tumors, the comparison to the references R_1 and R_2 yields 24 Dice indices.

3.3. Parameter setting

For each method, every parameter is optimized to obtain the best average Dice index over the whole dataset. The Dice index is chosen as a reference because it takes into account both the sensitivity and the precision.

The proposed algorithm (PBE+CDR) is used with a fixed ratio $\alpha/\beta = 1$, which means that the PBE term and log-likelihood term have equal importance (see Appendix A). The parameter κ_0 sets the inverse minimal length scale of the roughness expected for a lesion. By inspection of the reference contours, it is set to $\kappa_0 = 0.23$. The parameter λ is set to $\lambda = 10$. The segmentation is robust to changes in λ, for example $\lambda = 20$ yields similar results. The optimal smoothing parameter is $\gamma = 0.7$.

3.4. Comparison with other methods

We compare the proposed algorithm to two methods:

- The (no bd) method is the log-likelihood intensity segmentation without boundary terms [18] with optimal parameter $\gamma = 0.35$. The method (no bd) also plays the role of a comparison with the previous state-of-the-art method [17], which is based on a similar log-likelihood criteria. The difference is that [17] assumes a Rayleigh distribution function, and it has been shown that the non-parametric method has better accuracy [18]. Notice also that compared with Markov Random Fields methods such as [17], level-set methods provide smoother results with fewer isolated region artifacts.

- The (GAC) method is the log-likelihood intensity method with an additional GAC boundary term, as found in [23]. The parameters defined in section 2.3 are set to $\gamma = 0.35$ and $\epsilon = 5$ after optimization.

3.5. Results

Table 1 summarizes all results for the Dice index D, MAD, sensitivity S and precision P.

- The proposed method yields the best results in terms of Dice index D, MAD and sensitivity S.

- The method (no bd) has the best precision P, but poor sensitivity and lower MAD. This is because the (no bd) algorithm is too conservative: because the segmented area is small and far from the true boundaries, it has fewer false positives.

Figure 5 shows slices of the ultrasound image in 6 lesions, the results of segmentation and the reference contours in orange. The figure gives visual cues of the sensitivity score: the sensitivity is highest ($S = 1$) whenever the segmentation covers the entire reference volume. The proposed method has better sensitivity than the (GAC) segmentation, which has better sensitivity than the (no bd) segmentation - with statistically significant improvements, as discussed below.

Fig. 6 is a box plot of the Dice index, MAD and S for all cases - the average was given in Table 1. The proposed method compares favorably to (no bd) and (GAC) in terms of the MAD and the sensitivity S.

The significance of these observations is then qualified statistically with paired t-tests. As an example, one wants to assess whether the Dice coefficient is significantly different between the proposed method and the (no bd) method. A paired samples t-test is performed, to test whether the difference between the Dice indices in the two methods is significantly different from zero. More precisely, the test asserts whether the hypothesis of zero mean difference can be rejected at a given confidence level.

The paired t-test is performed for the different metrics (Dice, Sensitivity, MAD). Each method is compared with the other methods and with the intra-observer variation. Since for a given method a total of 3 paired t-tests are made, the default significance level (5%) is divided by 3 (1.7% confidence level) to rule out statistical issues due to multiple comparisons. The results of the significance test are shown in Fig. 7, where a symbol ✓ means that the difference is significant.

The significance tests of Fig. 7 show that the Dice coefficient is roughly similar for the different methods. This is probably related to the parameter search, which is made to provide the best Dice coefficient. The question becomes: which method has best sensitivity and lower MAD for a similar Dice index. Figure 7 also shows that the improvements of the proposed method in term of sensitivity S are relevant. For the proposed method the average is $S = 0.82$, whereas it is $S = 0.65$ for (no bd), a 26% improvement. Additionally, for the sensitivity, the hypothesis of equal means between the proposed method and the intra-observer variation can not be ruled out, meaning that their mean is not significantly different. Qualitatively, this means that the sensitivity is roughly as good as that of an expert.

Figure 8 is a scatter plot of the sensitivity S versus precision P for the three methods and the intra-observer variability. It illustrates the trade-off between sensitivity S (segment as much of the lesion area as possible) and precision P (only segment areas which are really part of the lesion). The method (no bd) has good precision P but very low sensitivity S (Fig. 8(a)), the method (GAC) has good sensitivity S (Fig. 8(b)), the proposed method has even better sensitivity S and better precision P compared with (GAC) (Fig. 8(c)). Figure 8(d) shows the intra-observer variability for comparison.

Figure 9 is a 3D representation of 6 different lesions and the local accuracy of the segmentation. The color map shows the local distance between the reference and the segmented volume. The distance is consistently lower using the proposed method than with (no bd) or (GAC) segmentation. This directly translates into a lower MAD as was found in Fig. 6(b) and Table 1.

Table 1: Average accuracy of the segmentation with the three methods (no bd) [18], GAC [23], the proposed method (PBE+CDR), and the intra-observer variability. The values indicated are the mean and standard deviation (±) over all cases.

	no bd	GAC	proposed	intra-obs.
D	0.74 ± 0.1	0.70 ± 0.15	**0.78** ± 0.1	0.84 ± 0.06
MAD (μm)	240 ± 140	330 ± 190	**200** ± 110	130 ± 60
S	0.65 ± 0.2	0.76 ± 0.12	**0.82** ± 0.14	0.86 ± 0.07
P	**0.93** ± 0.09	0.74 ± 0.3	0.80 ± 0.2	0.83 ± 0.08

4. Discussion

Let us comment on the accuracy and limitations of each method.

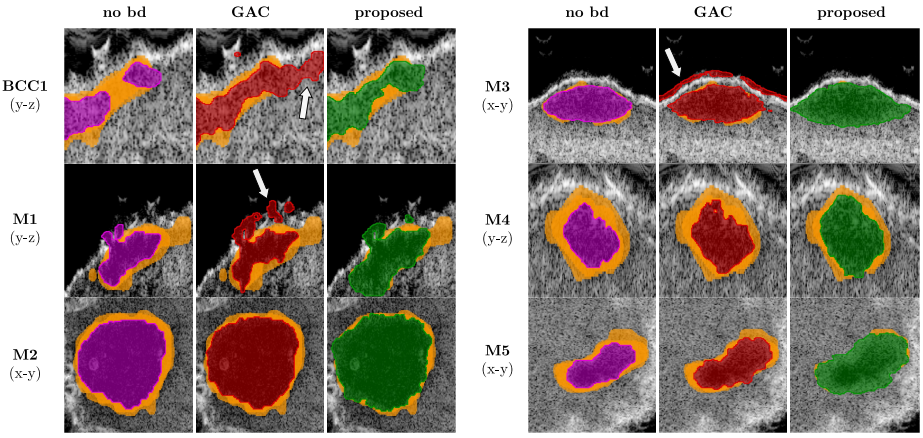

Figure 5: Slices of the 3D ultrasound images on one BCC (BCC1) and 5 melanoma (M1, M2, M3, M4, M5). The different columns represent the segmentation for the methods (no bd) [18] (purple), GAC [23] (red) and the proposed method (green), from left to right. The reference contours R_1 and R_2 are displayed as orange areas with half transparency (outside of the segmented contours). The orange areas are thus areas missed by the segmentation.

As it was said in the introduction, the reference method (no bd) [18] has good precision but low sensitivity, because it tends to underestimate the size of the lesions, as shown in Fig. 5, see also Fig. 8.

The (GAC) [23] method increases the sensitivity thanks to a better accuracy at the boundary. The energy E^{GAC} defined in section 2.3 drives the contour to maxima of the feature asymmetry $\text{FA}_{\mathbf{x}}$ map, as shown in Fig. 2. Since the Feature Asymmetry map is a good indicator of the edges of the lesion, the sensitivity of the segmentation is improved. However, the (GAC) term works via a local decrease of the regularization factor $g_{\mathbf{x}}^{\text{GAC}} = 1/(\epsilon + \text{FA}_{\mathbf{x}})$ near the maxima of the $\text{FA}_{\mathbf{x}}$ map, as shown in section 2.3. This gives rise to isolated artifacts around the lesion and less regular contours shown with white arrows in Fig. 5, for the cases BCC1, M1 and M3. Because of this, the sensitivity of (GAC) is better than that of (no bd), but the MAD is much higher (worse), see Fig. 6.

This observation led to the idea of designing a boundary term that does not act like a boundary term, but instead as a log-likelihood area term, the PBE term of section 2.3. This term helps the contour to expand closer to the boundaries of lesions, increasing the sensitivity, but does not create regularization artifacts like (GAC). The proposed method also uses the curvature-dependent regularization (CDR) of section 2.4, to avoid the curvature-driven effect on smooth boundaries of Fig. 3 or Fig. 4, responsible for the loss of sensitivity of the (no bd) segmentation. As is summarized in Table 1, Fig. 6, Fig. 8 and Fig. 9, the careful design of these terms provide an increase in sensitivity and decreases (improves) the MAD, compared with the (GAC) method.

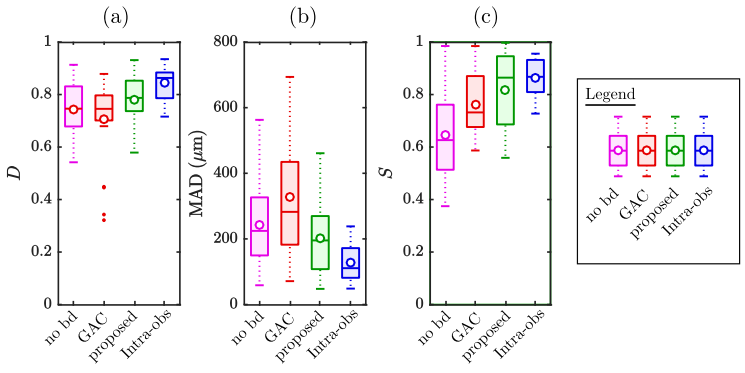

Figure 6: **(a)** Dice D, **(b)** MAD (μm) and **(c)** sensitivity S for the standard segmentation without boundary terms (no bd) [18] in purple, the GAC segmentation [23] in red, the proposed method in green and the intra-observer variability $D(R_1|R_2)$, MAD$(R_1|R_2)$ and $S(R_1|R_2)$ in blue.

Some additional results are not shown in the figures:

- It is shown above that the two proposed terms (PBE+CDR) improve the sensitivity. Further tests have shown that, using only one of the terms (PBE) or (CDR), e.g. setting either $\gamma = 0$ or $\beta = 0$ in (1), the sensitivity higher than with (no bd). The gain is optimal when both terms are combined as in the proposed (PBE+CDR) method.

- A case by case inspection of the metrics show that the sensitivity is actually better with the proposed method than with the (no bd) method [18], for each individual case in the dataset. This raises confidence that the observed improvements generalize beyond the available dataset.

Concerning computation time, the Markov Random Fields [17] are slower, one segmentation taking approximately one hour. On the other hand, the three methods (CDR+PBE), (no bd) and (GAC) compared here have a similar computation time of 40 s for a 3D image of 9 millions of voxels, thanks to the use of a coarse grid. Without grid, as in [23], the computation time of the (GAC) segmentation is of 20 minutes.

We now underline some limitations of the proposed method. Table 7 shows that the MAD is significantly higher for the proposed method than for the intra-observer MAD, and that the Dice is significantly lower, meaning that the method is less accurate than the expert and that it can be improved. One limitation is related to the original assumptions made in equation (2), which states that the intensity in the lesion derives from a single distribution $P(I_{\mathbf{x}}|A)$. This is problematic when the intensity distribution of some other region (say the gel area) is similar to the intensity distribution in the tumor. In such a case, artifacts occur such as those shown in Fig. 5 for the lesion M1, where small regions outside of the dermis are segmented as tumor regions. To avoid this, one may use supervised learning such as neural networks to learn more sophisticated

D				
no bd		×	×	✓$_1$
GAC	×		×	✓$_2$
proposed	×	×		✓$_3$
Intra-obs	✓$_1$	✓$_2$	✓$_3$	
	no bd	GAC	proposed	Intra-obs

MAD				
no bd		×	×	✓$_4$
GAC	×		✓$_5$	✓$_6$
proposed	×	✓$_5$		✓$_7$
Intra-obs	✓$_4$	✓$_6$	✓$_7$	
	no bd	GAC	proposed	Intra-obs

S				
no bd		✓$_8$	✓$_9$	✓$_{10}$
GAC	✓$_8$		✓$_{11}$	✓$_{12}$
proposed	✓$_9$	✓$_{11}$		×
Intra-obs	✓$_{10}$	✓$_{12}$	×	
	no bd	GAC	proposed	Intra-obs

Figure 7: Results of the statistical paired t-test for the rejection of the hypothesis of equal means. The proposed metrics (Dice D, MAD, Sensitivity S) for one method is compared with the metrics for the other methods and the intra-observer variation. ✓ means that the hypothesis is rejected - hence that the difference is estimated to be significant. × means that the hypothesis is not rejected. The p-value in the case of null hypothesis rejection is (with the number indicated in each case beside ✓): $p_1 = 2 \times 10^{-5}$, $p_2 = 2 \times 10^{-4}$, $p_3 = 7 \times 10^{-5}$, $p_4 = 1 \times 10^{-4}$, $p_5 = 4 \times 10^{-3}$, $p_6 = 8 \times 10^{-5}$, $p_7 = 4 \times 10^{-3}$, $p_8 = 5 \times 10^{-6}$, $p_9 = 8 \times 10^{-8}$, $p_{10} = 3 \times 10^{-6}$, $p_{11} = 2 \times 10^{-3}$, $p_{12} = 1.5 \times 10^{-3}$.

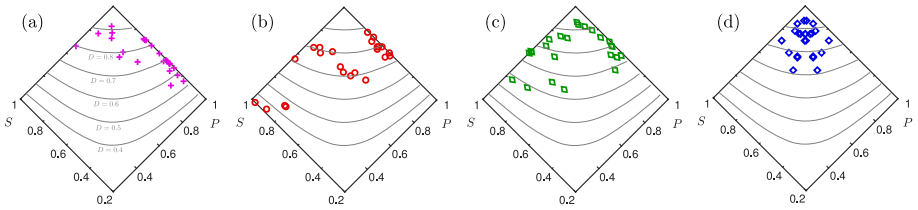

Figure 8: Sensitivity S versus precision P for different segmentation methods. For a good segmentation, both the sensitivity and the precision should be as close to one as possible. The Dice index D is related to P and S as $D = 2/(1/S + 1/P)$. Lines of constant Dice index are indicated as gray lines. (a) (no bd) segmentation [18]. The sensitivity is often too low. (b) (GAC) segmentation [23]. The precision is often too low. (c) Proposed method, with the best sensitivity/precision trade-off. (d) Intra-observer variability.

texture criteria, or one may add more geometric priors with a better assessment of the epidermis and regions above the skin. Such improvements are beyond the scope of this study.

We finally comment on the generality of the methods proposed here. The proposed boundary terms are not specific to the tumors studied here, and could thus be applied to other segmentation problems where the region of interest has intensity gradients on the boundary, a very common situation in medical imaging. The feature asymmetry is known to be robust for ultrasound images. The curvature-dependent regularization is even more general and may apply to any level-set method. It could for example be relevant for the segmentation of structures with tubular or irregular shapes, cases in which the standard regularization does not yield satisfying results. Furthermore, the same terms can be directly generalized from the level-set formalism to the equivalent convex segmentation algorithms, or the equivalent discrete min-cut problem.

The segmented volumes and the 3D ultrasound images of the dataset are

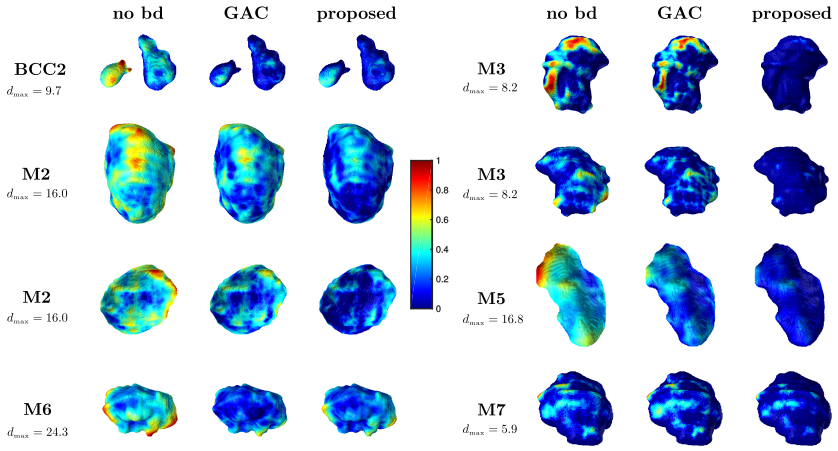

Figure 9: Color map of the local inaccuracy of the segmentation, on the 3D reference shape. Specifically, the color map is the point distance from the reference volume to the segmented shape. The three columns are the segmentation without boundary terms (no bd) [18], the GAC [23] and the proposed method. The range of the color scale is normalized to the maximum value for each lesion, red is the maximum distance $d_{\max}$ indicated for each case (in pixel, 1 pixel = 53 μm). The figure shows one BCC (BCC2) and 5 melanoma (M2, M3, M5, M6, M7). The melanomas M2 and M3 are shown under two different angles.

accessible online[1].

5. Conclusion

In this article, we have proposed a method based on two boundary terms to improve the segmentation of boundaries in 3D high-frequency ultrasound images of skin lesions. The first term is a conditional probabilistic boundary expansion (PBE) term, based on the phase asymmetry. The second term is a curvature-dependent regularization (CDR) term, which alleviates the curvature driven dynamics normally found in the level-set method. On the tested clinical dataset of 12 lesions, the combined method (PBE+CDR) improved the segmentation significantly. In particular, the sensitivity is improved in each case. The average sensitivity is increased from 0.65 to 0.82, a 26% improvement.

Acknowledgment

This work was funded by the ANR-14-LAB3-0006-01 LabCom AtysCrea and was supported by the LABEX CeLyA (ANR-10-LABX-0060) of Université de Lyon, within the "Investissements d'Avenir" program (ANR-11-IDEX-0007) operated by the French National Research Agency (ANR).

[1]Web demonstrator at: `http://www.atyscrea.insa-lyon.fr/en/demo_echo3D`, based on the *desk* library [32]

Appendix A. Gradient descent

In the standard way, the gradient descent (7) is first recast [33] to the form

$$\partial_t \phi_{\mathbf{x}} = |\nabla \phi| \, (\alpha f_{\mathbf{x}}^{\text{int}} + \beta f^{\text{PBE}} + \gamma f_{\mathbf{x}}^{\text{CDR}}) \tag{A.1}$$

The above equations are solved with Additive Operator Splitting (AOS) [34] on a narrow-band region Γ within a distance T_s of the contour. The parameters α and β are dynamically adapted at each step k according to:

$$\alpha^k = \frac{\alpha T_s}{\Delta t \ \max_{\mathbf{x}\in\Gamma_k} |\alpha f_{\mathbf{x}}^{\text{int}} + \beta f_{\mathbf{x}}^{\text{PBE}}|} \tag{A.2}$$

$$\beta^k = \frac{\beta T_s}{\Delta t \ \max_{\mathbf{x}\in\Gamma_k} |\alpha f_{\mathbf{x}}^{\text{int}} + \beta f_{\mathbf{x}}^{\text{PBE}}|} \tag{A.3}$$

$$\Gamma^k = \{\mathbf{x} \mid \ |\phi_{\mathbf{x}}| < T_s \ \ \& \ \ \text{sign}(\phi_{\mathbf{x}}(\alpha f_{\mathbf{x}}^{\text{int}} + \beta f_{\mathbf{x}}^{\text{PBE}})) < 0\} \tag{A.4}$$

Γ^k is a narrow-band region within a distance T_s of the contour, and is restricted to points that may change region according to gradient descent term ($\text{sign}(\phi_{\mathbf{x}}(\alpha f_{\mathbf{x}}^{\text{int}} + \beta f_{\mathbf{x}}^{\text{PBE}}) < 0$). The value of α^k and β^k in (A.2) is chosen such that a point at the boundary of Γ^k changes region, if and only if, the value of f^{int} is maximal at this point, and such that at least one pixel changes region at every step.

Algorithm 1 enumerates the main steps of the gradient descent. In the iterative loop, at step 3, a fast-marching algorithm [33] resets the level-set function $\phi_{\mathbf{x}}$ to $|\nabla\phi| = 1$ for $\mathbf{x} \in X$, $\phi_{\mathbf{x}} = 0$ for $\mathbf{x} \in \partial A$. The evolution step (7) is then performed alternately, in step 6, and then on the regularization term f^{CDR} in step 7 with an AOS semi-implicit Euler scheme, which is stable for arbitrary time steps. In the following, the time step is fixed to $\Delta t = 1$ (only the product $\gamma \, \Delta t$ enters Step 7 and the threshold is set to $T_s = 2$. The remaining parameters are γ, which sets the degree of smoothness and the ratio α/β, which sets the relative weight of the boundary term and the intensity term.

Algorithm 1 Gradient descent solver

1: Manual initialization of $\phi_{\mathbf{x}}^1$
2: **for** $k = 1 \ldots \infty$ **do**
3: Reset $|\nabla \phi^k| = 1$
4: Set α^k, β^k according to (A.2)
5: Update $\kappa_{\mathbf{x}}$, $g_{\mathbf{x}}$, $\hat{P}(I|A)$, $\hat{P}(I|B)$
6: Let $\phi_{\mathbf{x}} \leftarrow \phi_{\mathbf{x}} + \Delta t \, |\nabla\phi| \, (\alpha_k f_{\mathbf{x}}^{\text{int}} + \beta_k f_{\mathbf{x}}^{\text{PBE}})$ for $\mathbf{x} \in \Gamma^k$
7: Let $\phi_{\mathbf{x}}^{k+1} \leftarrow \phi_{\mathbf{x}} + \gamma \, \Delta t |\nabla\phi| f_{\mathbf{x}}^{\text{CDR}}$ for all $\mathbf{x}$
8: **end for**

References

[1] H. W. Rogers, M. A. Weinstock, A. R. Harris, M. R. Hinckley, S. R. Feldman, A. B. Fleischer, B. M. Coldiron, Incidence estimate of nonmelanoma skin cancer in the united states, 2006, Archives of dermatology 146 (2010) 283–287.

[2] N. E. Davidson, S. A. Armstrong, L. M. Coussens, M. R. Cruz-Correa, R. J. DeBerardinis, J. H. Doroshow, M. Foti, P. Hwu, T. W. Kensler, M. Morrow, et al., Aacr cancer progress report 2016, Clinical Cancer Research 22 (2016) S1–S137.

[3] J. K. Robinson, Sun exposure, sun protection, and vitamin D, Jama 294 (2005) 1541–1543.

[4] C. M. Balch, J. E. Gershenwald, S.-j. Soong, J. F. Thompson, M. B. Atkins, D. R. Byrd, A. C. Buzaid, A. J. Cochran, D. G. Coit, S. Ding, et al., Final version of 2009 AJCC melanoma staging and classification, Journal of clinical oncology 27 (2009) 6199–6206.

[5] F. J. Bath-Hextall, W. Perkins, J. Bong, H. C. Williams, Interventions for basal cell carcinoma of the skin, The Cochrane Library (2007).

[6] S. González, M. Gill, A. C. Halpern, Reflectance confocal microscopy of cutaneous tumors: an atlas with clinical, dermoscopic and histological correlations, CRC Press, 2008.

[7] S. Bassoli, A. Maurichi, M. Rodolfo, A. Casari, S. Frigerio, G. Pupelli, F. Farnetani, G. Pelosi, M. Santinami, G. Pellacani, CDKN2A and MC1R variants influence dermoscopic and confocal features of benign melanocytic lesions in multiple melanoma patients, Experimental dermatology 22 (2013) 411–416.

[8] A. Jambusaria-Pahlajani, C. D. Schmults, C. J. Miller, D. Shin, J. Williams, S. K. Kurd, J. M. Gelfand, Test characteristics of high-resolution ultrasound in the preoperative assessment of margins of basal cell and squamous cell carcinoma in patients undergoing mohs micrographic surgery, Dermatologic Surgery 35 (2009) 9–16.

[9] E. van Loo, K. Mosterd, G. A. Krekels, M. H. Roozeboom, J. U. Ostertag, C. D. Dirksen, P. M. Steijlen, H. M. Neumann, P. J. Nelemans, N. W. Kelleners-Smeets, Surgical excision versus Mohs' micrographic surgery for basal cell carcinoma of the face: A randomised clinical trial with 10 year follow-up, European Journal of Cancer 50 (2014) 3011 – 3020.

[10] J. V. Moore, E. Allan, Pulsed ultrasound measurements of depth and regression of basal cell carcinomas after photodynamic therapy: relationship to probability of 1-year local control, British Journal of Dermatology 149 (2003) 1035–1040.

[11] T. D. Desai, A. D. Desai, D. C. Horowitz, F. Kartono, T. Wahl, The use of high-frequency ultrasound in the evaluation of superficial and nodular basal cell carcinomas, Dermatologic Surgery 33 (2007) 1220–1227.

[12] L. Machet, L. Samimi, G. Georgesco, Y. Mourtada, M. Naouri, J.-M. Grégoire, F. Ossant, F. Patat, L. Vaillant, High resolution ultrasound imaging of melanocytic and other pigmented lesions of the skin, in: M. Tanabe (Ed.), Ultrasound Imaging, InTech, 2010.

[13] M. Mete, N. M. Sirakov, Dermoscopic diagnosis of melanoma in a 4D space constructed by active contour extracted features, Computerized Medical Imaging and Graphics 36 (2012) 572 – 579.

[14] J. E. Mayer, S. M. Swetter, T. Fu, A. C. Geller, Screening, early detection, education, and trends for melanoma: current status (2007-2013) and future directions: Part i. epidemiology, high-risk groups, clinical strategies, and diagnostic technology, Journal of the American Academy of Dermatology 71 (2014) 599–e1.

[15] P. Bourne, C. Rosendahl, J. Keir, A. B. Cameron, A diagnostic algorithm for skin cancer diagnosis combining clinical features with dermatoscopy findings. dermatol pract conc. 2012; 2 (2): 12, 2007.

[16] X. Yuan, N. Situ, G. Zouridakis, A narrow band graph partitioning method for skin lesion segmentation, Pattern Recognition 42 (2009) 1017–1028.

[17] M. Pereyra, N. Dobigeon, H. Batatia, J. Tourneret, Segmentation of skin lesions in 2D and 3D ultrasound images using a spatially coherent generalized rayleigh mixture model, Medical Imaging, IEEE Transactions on 31 (2012) 1509–1520.

[18] B. Sciolla, L. Cowell, T. Dambry, B. Guibert, P. Delachartre, Segmentation of skin tumors in high-frequency 3D ultrasound images, Ultrasound in medicine & biology 43 (2017) 227–238.

[19] R. Malladi, J. Sethian, Image processing: Flows under min/max curvature and mean curvature, Graphical Models and Image Processing 58 (1996) 127 – 141.

[20] P. Kovesi, Symmetry and asymmetry from local phase, in: Tenth Australian Joint Conference on Artificial Intelligence, 1997, pp. 2–4.

[21] M. Felsberg, G. Sommer, The monogenic signal, Signal Processing, IEEE Transactions on 49 (2001) 3136–3144.

[22] K. Rajpoot, V. Grau, J. Noble, Local-phase based 3d boundary detection using monogenic signal and its application to real-time 3-d echocardiography images, in: Biomedical Imaging: From Nano to Macro, 2009. ISBI '09. IEEE International Symposium on, 2009, pp. 783–786.

[23] W. Qiu, J. Yuan, J. Kishimoto, J. McLeod, Y. Chen, S. de Ribaupierre, A. Fenster, User-guided segmentation of preterm neonate ventricular system from 3D ultrasound images using convex optimization, Ultrasound in Medicine & Biology 41 (2015) 542 – 556.

[24] A. Belaid, D. Boukerroui, Y. Maingourd, J.-F. Lerallut, Phase-based level set segmentation of ultrasound images, Information Technology in Biomedicine, IEEE Transactions on 15 (2011) 138–147.

[25] M. Marino, F. Veronesi, C. Corsi, Fully automated assessment of left ventricular volumes and mass from cardiac magnetic resonance images, in: Engineering in Medicine and Biology Society (EMBC), 2014 36th Annual International Conference of the IEEE, 2014, pp. 1079–1082.

[26] F. Catté, P.-L. Lions, J.-M. Morel, T. Coll, Image selective smoothing and edge detection by nonlinear diffusion, SIAM Journal on Numerical Analysis 29 (1992) 182–193.

[27] M. Burger, F. Haußer, C. Stöcker, A. Voigt, A level set approach to anisotropic flows with curvature regularization, Journal of computational physics 225 (2007) 183–205.

[28] J. Kim, J. Fisher, A. Yezzi, M. Cetin, A. Willsky, A nonparametric statistical method for image segmentation using information theory and curve evolution, Image Processing, IEEE Transactions on 14 (2005) 1486–1502.

[29] I. Selesnick, R. Baraniuk, N. Kingsbury, The dual-tree complex wavelet transform, Signal Processing Magazine, IEEE 22 (2005) 123–151.

[30] V. Caselles, R. Kimmel, G. Sapiro, Geodesic active contours, in: Computer Vision, 1995. Proceedings., Fifth International Conference on, 1995, pp. 694–699.

[31] T. Chan, L. Vese, Active contours without edges, Image Processing, IEEE Transactions on 10 (2001) 266–277.

[32] H. Jacinto, R. Kéchichian, M. Desvignes, R. Prost, S. Valette, A web interface for 3D visualization and interactive segmentation of medical images, in: Proceedings of the 17th International Conference on 3D Web Technology, 2012, pp. 51–58.

[33] Y. Zhang, B. Matuszewski, L. Shark, C. Moore, Medical image segmentation using new hybrid level-set method, in: BioMedical Visualization, 2008. MEDIVIS '08. Fifth International Conference, 2008, pp. 71–76.

[34] J. Weickert, B. Romeny, M. Viergever, Efficient and reliable schemes for nonlinear diffusion filtering, Image Processing, IEEE Transactions on 7 (1998) 398–410.